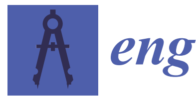

MDPI

*Article*

# Generalized Damping Model for MEMS Oscillators from Molecular to Viscous Flow Regime

**Tobias Zengerle [1,*], Abdallah Ababneh [2] and Helmut Seidel [1]**

[1] Department of Physics, Saarland University, 66123 Saarbrücken, Germany; seidel@lmm.uni-saarland.de
[2] Electronic Engineering Departement, Hijjawi Faculty for Engineering Technology, Yarmouk University, Irbid 21163, Jordan; a.ababneh@yu.edu.jo
* Correspondence: t.zengerle@lmm.uni-saarland.de

**Abstract:** In this study, we investigate the damping phenomena acting on piezoelectrically driven MEMS oscillators. Three different geometrical shapes of MEMS oscillators are presented, including cantilevers, bending oscillators, and paddle oscillators. An analytical model for their resonance frequencies is derived. The bending modes of these micro-oscillator structures are characterized regarding their resonance frequency and their quality factor as a function of the ambient pressure in a nitrogen atmosphere as well as the dependence on the distance to a neighboring plate representing a geometrical boundary (e.g., to the package or to the mounting). The investigations cover a pressure range from $10^{-3}$ mbar up to 900 mbar and a gap width from 150 µm to 3500 µm. Consequently, a Knudsen number range over six orders of magnitude from 100 to $10^{-4}$ is covered. The measurement data are evaluated with a generalized damping model consisting of four parts representing the individual damping mechanisms (intrinsic, molecular, transitional, and viscous). The evaluated parameters are analyzed as a function of the resonance frequency and the gap width. The data reveal an exponential growing saturation behavior, which is determined by two characteristic lengths, being correlated with the viscous and the thermal boundary layer thickness, respectively. This leads to an estimation of the strength and of the range of the damping effect just by calculating the boundary layer thicknesses given by the resonance frequency and the gas properties. From these results, we gain fundamental insights on the viscous and transitional damping mechanisms as well as on the intrinsic losses. In conclusion, a basic concept is provided to reduce the damping of micro-oscillator bending modes and thus increase the quality factor. Additionally, the results are supported by finite element simulations revealing the temperature and pressure distribution within the gap.

**Keywords:** *Q* factor; damping model; transitional flow regime; viscous flow regime; MEMS oscillator; bending modes

check for updates

**Citation:** Zengerle, T.; Ababneh, A.; Seidel, H. Generalized Damping Model for MEMS Oscillators from Molecular to Viscous Flow Regime. *Eng* **2022**, *3*, 124–141. https://doi.org/10.3390/eng3010011

Academic Editor: Van Dau

Received: 18 January 2022
Accepted: 23 February 2022
Published: 25 February 2022

**Publisher's Note:** MDPI stays neutral with regard to jurisdictional claims in published maps and institutional affiliations.

**Copyright:** © 2022 by the authors. Licensee MDPI, Basel, Switzerland. This article is an open access article distributed under the terms and conditions of the Creative Commons Attribution (CC BY) license (https://creativecommons.org/licenses/by/4.0/).

## 1. Introduction

MEMS oscillators are widely used in our technological world and are found in a variety of applications [1–5]. Based on their operating principle, the oscillators can be divided into two classes: electrostatic excitation and piezoelectric excitation. The advantages of electrostatic excitation include a high-quality factor *Q* and good frequency stability, especially for frequency timing applications [6]. However, disadvantages are a high operating voltage, occurring nonlinearities, and difficult processing due to the narrow gaps that are required between the two capacitor plates. Piezoelectric oscillators, on the other hand, are characterized by low operating voltage, high electromechanical coupling, and simple CMOS-compatible batch processing since there is no requirement for a gap. However, a disadvantage compared to electrostatic excitation is the lower *Q* factor and the associated impact on oscillator performance, such as resolution and frequency stability. For this reason, an important area of research is to increase the quality factor of piezoelectric oscillators [7]. This includes an enhancement of the material-related intrinsic quality factor, as well as the

reduction of extrinsic damping effects, being related to environmental ambient pressure and geometrical boundaries [8,9]. In many applications, MEMS oscillators are operated under various ambient conditions, e.g., in a liquid, in a gas atmosphere, or encapsulated under vacuum conditions. Furthermore, the distance of the micro-oscillator to a mounting or to a package is an important factor [10–12]. Therefore, we investigate the influence of an encapsulation package under various ambient pressure conditions and experimentally correlate them with the damping effects.

The overall quality factor of a micro-oscillator is determined by four different damping mechanisms. Therefore, in the first step, the main loss factor must be determined, which subsequently has to be minimized to increase the overall quality factor of the MEMS oscillator. At low pressure ($p$ = 0.01 mbar), the intrinsic damping losses are dominant and the extrinsic losses due to the gas atmosphere can be neglected. The extrinsic damping mechanisms are subdivided further, corresponding to the Knudsen number, which is defined by the ambient pressure and the gap width. In the low-pressure range, with a respectively high Knudsen number ($Kn > 1$), molecular flow damping dominates, whereas in the high-pressure range up to atmospheric pressure and beyond viscous flow damping is defined ($Kn < 0.01$) [13]. In between, the transitional flow regime is encountered, where the damping is described by thermal wave resonance effects [14]. Within this paper, we examine a generalized damping model for various oscillator structure shapes with different coverage sizes of the piezoelectric thin film layer. The oscillators are characterized over a large pressure range and over a varying gap width. The generalized damping model shows good agreement with the experimental data, covering six orders of magnitude for the Knudsen number. Additionally, numerical simulations are performed to model the pressure and temperature distribution supporting the found damping fundamentals. With the help of the results, design rules for an optimization of the quality factor on the dependence of the gap width to the package are derived, based only on the resonance frequency.

## 2. Generalized Damping Model

### *2.1. MEMS-Oscillator*

The investigated MEMS oscillator structures are shown in Figure 1 and are subdivided into three classes regarding their shape: paddle oscillator (PO), bending oscillator (BO), and cantilever oscillator (CO). The resonance frequency of such MEMS oscillators can be derived by the theory of an externally driven damped harmonic oscillator [15]. This results in the fundamental resonance frequency $f_\mathrm{r}$:

$$f_\mathrm{r} = \frac{1}{2\pi}\sqrt{\frac{k}{m}}, \tag{1}$$

where $k$ and $m$ denote the spring constant, and the mass of the MEMS oscillator, respectively.

The mass of the MEMS oscillator can be calculated easily by the density–volume product, and the spring constant is given by solid mechanics [16]:

$$k_\mathrm{B} = \frac{3E_\mathrm{Si}I}{L^3} = \frac{E_\mathrm{Si}BT^3}{4L^3}, \tag{2}$$

with Young's modulus $E_\mathrm{Si}$ of the MEMS oscillator, as well as the moment of inertia $I$, the length $L_\mathrm{B}$, the width $B_\mathrm{B}$ and the thickness $T$ of the beam.

For the PO and BO structures, we assume two parallel-connected beam spring constants ($k = k_\mathrm{B}||k_\mathrm{B} = 2k_\mathrm{B}$) with the length $L = L_\mathrm{B} + L_\mathrm{O}$, and width $B = B_\mathrm{B}$. For the CO structures, the length $L$ and the width $B$ are directly given by the oscillator dimension $L_\mathrm{O}$ and $B_\mathrm{O}$.

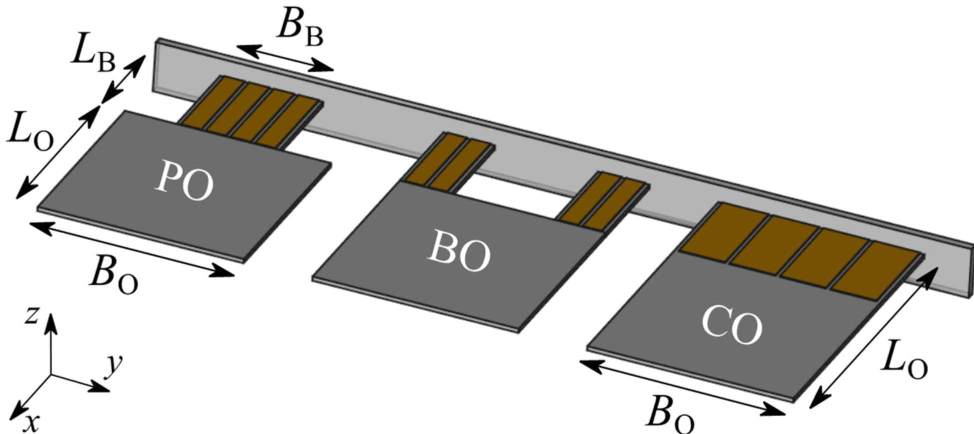


**Figure 1.** Schematic 3D view on the investigated MEMS oscillator structures. From left to right: paddle oscillator PO, bending oscillator BO, and cantilever oscillator CO. The oscillators with thickness $T$ are actuated with piezoelectric AlN elements, which are covered with gold electrodes. Microscope images of the fabricated micro-oscillators can be found in Appendix A.

Moreover, we scale the mass $m$ of the MEMS oscillator by a factor $\alpha$ attributing the effect that not the entire structure is vibrating [17]. Therefore, the effective mass $m_{\text{eff}} = \alpha \cdot m$ is used in the following calculations.

Taking everything into account, this leads to the resonance frequency of the MEMS oscillator as a function of its geometry and material properties:

$$f_{\text{r}} = \frac{1}{2\pi} \begin{cases} T\sqrt{\frac{E_{\text{Si}}}{2\alpha\rho_{\text{Si}}} \frac{B_{\text{B}}}{(L_{\text{B}}+L_{\text{O}})^3\,(2B_{\text{B}}L_{\text{B}}+B_{\text{O}}L_{\text{O}})}} \text{ for PO/BO} \\ \frac{T}{2L_{\text{O}}^2}\sqrt{\frac{E_{Si}}{\alpha\rho_{Si}}} \text{ for CO} \end{cases}. \quad (3)$$

This calculation is valid for the resonance frequency of the first fundamental bending mode (BM) of the MEMS oscillator. The resonance frequency of the higher bending modes $f_n$ with mode number $n$ can be calculated as a multiple of the squared eigenvalue $\lambda_n$ [18]:

$$f_n = \lambda_n{}^2 f_{\text{r}}. \quad (4)$$

The eigenvalue $\lambda_n$ is given by 1.88; 4.69; 7.86; 11.00 for the first four bending modes [17]. This analytical approach will be discussed in the experimental section, regarding the accuracy of the description as well as the influence of the different geometric shapes on the scale factor $\alpha$, which is experimentally investigated.

*2.2. Quality Factor Q*

The second characteristic value besides the resonance frequency of a MEMS oscillator is the quality factor $Q$. This is a measure for the damping and is defined by the ratio of the total energy of an oscillator $E$ to the energy dissipation per cycle $\Delta E$. Its value can be measured from a resonance curve plot using the 3dB bandwidth $\Delta f_{3\text{dB}}$ [19]:

$$Q = \frac{E}{\Delta E} = \frac{f_n}{\Delta f_{3\text{dB}}}. \quad (5)$$

The experimentally measured quality factor always represents a combination of several individual damping mechanisms, which can be combined via the superposition principle.

The damping phenomena can be divided into two classes, the material related intrinsic ones, and the extrinsic ones from the surrounding gas atmosphere:

$$Q_{\text{exp}} = \left(\frac{1}{Q_{\text{int}}} + \frac{1}{Q_{\text{ext}}}\right)^{-1} = \left(\frac{1}{Q_{\text{int}}} + \underbrace{\frac{1}{Q_{\text{mol}}} + \frac{1}{Q_{\text{trans}}} + \frac{1}{Q_{\text{vis}}}}_{\frac{1}{Q_{\text{gas}}}}\right)^{-1}. \quad (6)$$

The intrinsic damping losses are independent of the external pressure and are determined by anchor losses [20], by the residual stress of the piezoelectric layer [21], and by thermoelastic damping effects [22]. Which of the three types of damping is dominant depends on the resonance frequency and on the bending mode.

The extrinsic damping influences can be further subdivided according to several flow regimes with respect to the Knudsen number $Kn$. The Knudsen number is given by the ratio of the mean free path $l_{\text{mfp}}$ to a representative length scale $l^*$. In the context of the investigations, the Knudsen number is changed on the one hand by the pressure which influences the mean free path, and on the other hand by the representative length scale which can be adjusted by a variable gap width $h$.

For the different individual flow regimes, descriptions of the damping behavior in the literature are available which are summarized in a more generalized damping model. In the molecular flow regime ($Kn > 1$), the quality factor can be described by a reciprocal dependency on the external pressure which was expanded by Bao et al. with a linear gap width $h$ dependency [23,24] (valid for small gap widths [25]):

$$Q_{\text{mol}} = \frac{\xi_{\text{mol}}(h)}{p}. \quad (7)$$

The other dependencies on the geometric shape, the size of the oscillator, the gas atmosphere, and the ambient temperature are summarized in the fit parameter $\xi_{\text{mol}}$ [bar].

For low Knudsen numbers ($Kn < 0.01$), the quality factor can be calculated for the viscous flow regime based on the Navier–Stokes equations under some simplifications (assumption of the MEMS oscillator as a chain of spheres/discs [26,27]). The result of these theories is a viscous quality factor exhibiting a dependency to the reciprocal square root of the external pressure:

$$Q_{\text{vis}} = \frac{\xi_{\text{vis}}(h)}{\sqrt{p}}. \quad (8)$$

The fit parameter $\xi_{\text{vis}}$ [bar$^{0.5}$] combines the influence of the geometry, the gas atmosphere, and temperature on the viscous quality factor. Dependence of the quality factor on the gap width is not covered by any of these works, except for the squeeze film regime, and is therefore specifically investigated in our work.

The transitional flow regime in-between the two previously presented flow regimes can be described by the resonance effect of thermal waves. The quality factor is described by a parabola-shaped function with a vertex located at the thermal wave resonance point where the mechanical resonance frequency $f_n$, matches with the thermal frequency of the gas locked within the gap width $f_{\text{th}}$. Here, the thermal frequency of the gas depends on its thermal diffusivity, which is changed by the external pressure, as well as on the adjusted gap width. The mathematical description of the quality factor plot of the transitional flow regime is as follows:

$$Q_{\text{trans}} = \xi_{\text{trans}}(h)\frac{f_n \cdot f_{\text{th}}}{f_n{}^2 + f_{\text{th}}{}^2}, \text{ with } f_{\text{th}} = \frac{B_{\text{trans}}}{\sqrt{p}}. \quad (9)$$

Further elaboration on this theory including the fit parameters $\xi_{\text{trans}}$ [1] and $B_{\text{trans}}$ [Hz·mbar$^{0.5}$] can be found in [14]. In previous works [14,25] and in Appendix B, the process

steps of the sensor fabrication and the experimental procedure of recording resonance curves for the extraction of the quality factor and resonance frequency are described.

## 3. FEM Simulations

In addition to the analytical description and the experimental investigation of the MEMS oscillators, finite element (FEM) simulations were performed for modeling the temperature and pressure distribution within the gap caused by the oscillator movement and also for determining the thickness of the oscillator.

In the oscillator manufacturing process, the thickness of the oscillators is determined by a time-controlled wet chemical etching process in a KOH solution. This process is affected by variations on the order of $\pm 3$ µm in the targeted oscillator thickness. For this reason, the thickness is determined numerically in COMSOL Multiphysics 5.4 with the solid mechanics' module using an eigenfrequency study of the MEMS oscillator [28]. The exact thickness of one micro-oscillator structure was measured by scanning electron microscopy (SEM). For this method of investigation, however, a thin Au layer is necessary for the conduction of the electrons, after which the oscillator is no longer suitable for further measurements. As an example, an SEM image is attached in Appendix A (see Figure A1d) and confirms the range of thickness of the micro-oscillators.

The pressure and temperature distribution within the gap are modeled by coupling the oscillator movement with the surrounding fluid using an adiabatic and no-slip boundary condition. The geometrical boundary at the top is a fixed plate placed in a defined spacing from the micro-oscillator. It possesses a nearly infinite heat capacity (relative to the amount of heat produced by the micro-oscillator movement) and is therefore modeled by an isothermal wall. Towards the bottom, the micro-oscillator is not confined, which is represented by the spherical wave radiation boundary condition. The behavior of the fluid is described by a linearized Navier–Stokes equation, which is valid for the continuum regime ($Kn < 0.1$). Furthermore, we use the continuity equation and the energy equation for fluids. The complete set of equations can be found in [14].

As a result, we obtain the pressure distribution and temperature distribution within the gap for the individual bending modes and geometric shapes. No significant difference between the distributions of the individual geometric shapes PO, BO, and CO is observed. Therefore, we only illustrate the distributions of a CO structure for the first three bending modes.

Figure 2a indicates a pressure increase $\Delta p$ as well as the resulting temperature rise $\Delta T$ within the gap due to the compression by the MEMS oscillator. Correspondingly, the same behavior in the opposite direction (expansion leading to pressure and temperature drop) can be observed on the bottom side. Furthermore, an asymmetry between the upper and the lower side is significant due to the spatial limitation of the gap towards the top. This asymmetry in the distributions decreases with increasing mode number and disappears almost completely up to the 3rd BM. From this, it can be concluded that the range of an interaction of the oscillator with a spatial boundary decreases with the mode number, respectively, with the resonance frequency.

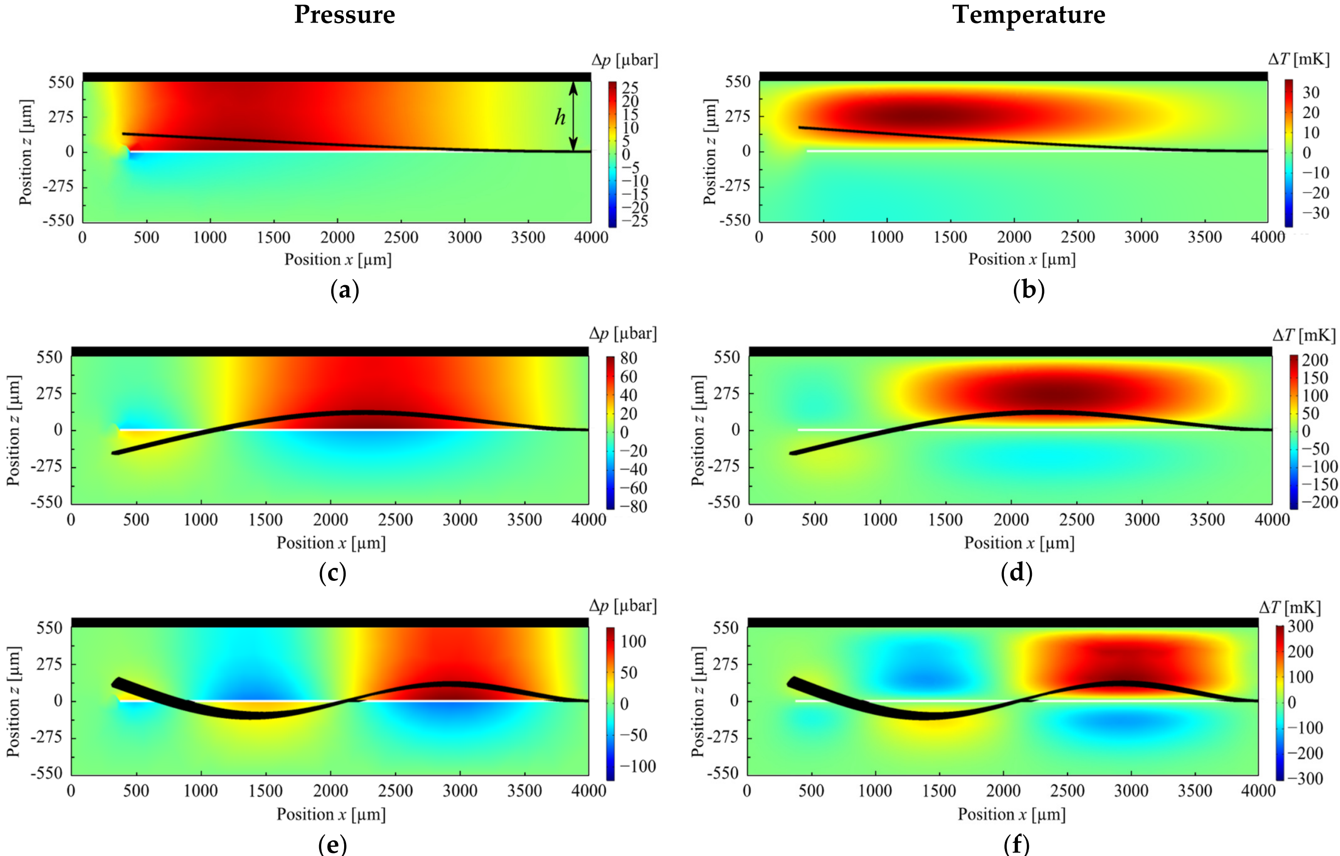


**Figure 2.** FEM-simulated pressure and temperature distribution for CO1 (*cf.* Table 1) at a gap width of 550 µm. In (**a**,**c**,**e**), the pressure distribution of the 1st, 2nd, and 3rd BM is displayed, respectively. In (**b**,**d**,**f**), the corresponding temperature distribution of the 1st, 2nd, and 3rd BM is shown. The ambient values are indicated by a green color. Deviations to the top are shown by red, or to the bottom by blue. The oscillator deflection (black) of the bending mode is shown enlarged and not to scale.

## 4. Experimental Results

Figure 3 shows a composition of the experimentally-measured quality factor $Q_{\text{exp}}$ consisting of the individual damping components, according to the theory section. The data show the quality factor plots for the 1st BM of the three different geometries and the 3rd BM of sensor BO for a gap width of 550 µm in a nitrogen atmosphere.

The fitting of the composition of the four different damping mechanisms was performed by a LabView nonlinear fitting tool. The quality of the fitting procedure was ensured by the coefficient of determination $R^2$ which was exceeding the value of 0.99 for all cases ($R^2$ = 1 is representing a perfect match between the experimental data and the theoretical fit.) The relative deviation of the fit model to the experimental data is in the range of 5%. Consequently, a very good agreement between the fitted quality factor $Q_{\text{fit}}$ and the experimental data over the entire pressure range can be achieved. The extrinsic gas part of the quality factor $Q_{\text{gas}}$ is calculated by subtracting the intrinsic damping and then is inserted additionally. Subsequently, for each gap width and mode, a set of parameters is obtained.

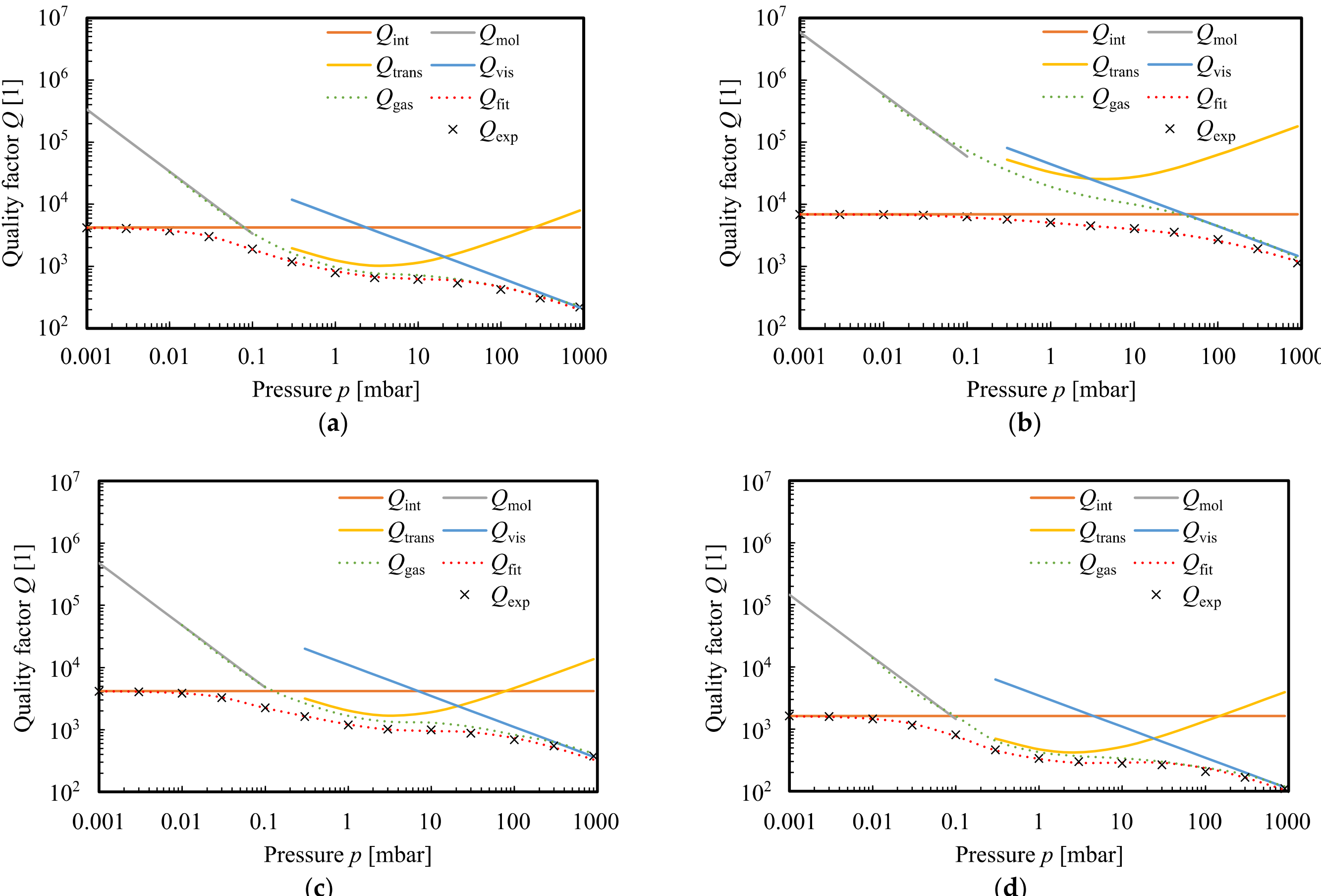


**Figure 3.** Reconstruction of the experimentally-measured quality factor plot $Q_{exp}$ as function of the ambient pressure. The total quality factor $Q_{fit}$ is composed of the individual damping mechanisms and shows very good agreement over the entire range from molecular to viscous flow regime for the 1st BM (**a**) and for the 3rd BM (**b**) of MEMS oscillator BO3 as well as for the 1st BM of the micro-oscillators PO1 (**c**) and CO1_33 (**d**). The data are measured at a gap width $h$ = 550 µm in an $N_2$ atmosphere.

In Figure 4a, the quality factor plot of micro-oscillator BO3 is depicted for the fundamental BM and the next higher bending modes up to a mode number of $n$ = 5. The strong decrease in the quality factor of the first BM in the medium pressure range is particularly noticeable. This is due to the stronger damping in the molecular flow regime (up to $p$ = 0.1 mbar) and due to the high thermal losses in the transitional flow regime caused by standing thermal waves [14]. The first bending mode also has the largest oscillation amplitude, which results in a stronger interaction with the surrounding gas atmosphere and, accordingly, to larger damping losses. The strength of the damping decreases with the mode number and is mainly visible in the viscous flow regime. For mode 5, the intrinsic damping is very pronounced, which leads to a masking of the extrinsic damping losses.

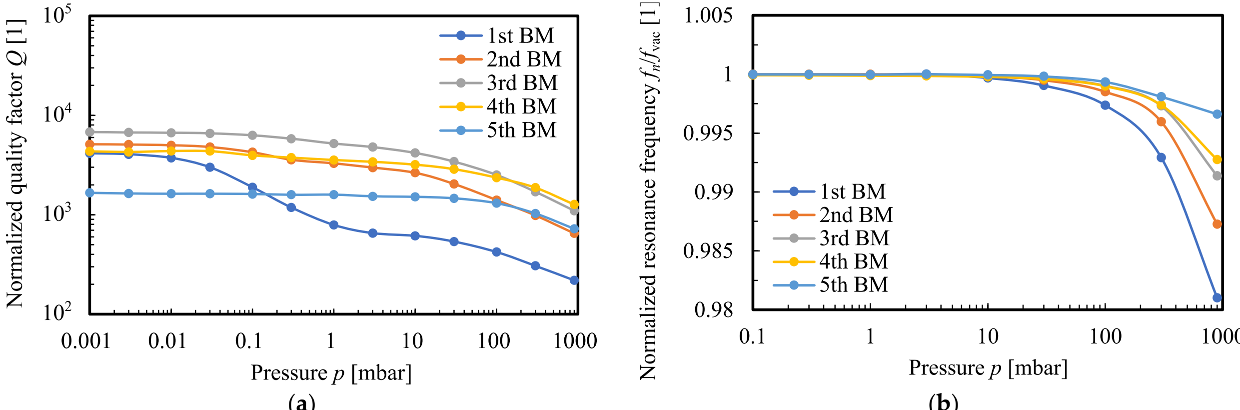


**Figure 4.** Quality factor plot (**a**) and normalized resonance frequency plot (**b**) as function of the ambient pressure of MEMS oscillator BO3 for the first five bending modes. The resonance frequency is normalized on the high vacuum value (at $p$ = 0.001 mbar). All data are recorded for a gap width of $h$ = 550 µm in an $N_2$ atmosphere.

For all bending modes, the strong damping in the viscous flow regime is common, which leads to a decrease in the quality factor as well as to a reduction of the resonance frequency (see Figure 4b). The highest shift of the resonance frequency due to the strongest damping can also be seen in the 1st BM. The other modes are sorted according to the mode number.

In addition to the quality factor, the resonance frequency of the fundamental mode, as well as the higher bending modes of the MEMS oscillators, are investigated. The frequencies are measured in the vacuum range at 0.001 mbar and then associated with the bending modes using a laser Doppler vibrometer. Besides the bending modes there are other modes, such as torsional oscillations or more complex roof-tile-shaped modes, which are not considered in this work. All electrically-measured bending modes are summarized in Appendix C. Based on the fundamental mode, the thickness of the MEMS oscillator is derived by means of FEM simulation. The results are shown in Table 1. The MEMS oscillators BO1, BO2, BO3, PO1, and PO2 were fabricated on a wafer with a target thickness of 20 µm and the CO structures on a second wafer with a target thickness of 10 µm. These thickness values could be found numerically and are in the range of the variations of the etching process.

**Table 1.** Listing of all investigated MEMS oscillator geometries and their dimensions. The thickness T is obtained from numerical simulations and the scale factor $\alpha$ is determined by applying best fit method of Equation (3) to resonance frequency plot shown in Figure 5. The Young's modulus $E_{Si}$ = 130 GPa and density $\rho_{Si}$ = 2.330 g/cm$^3$ are taken from [29].

| Name | $L_O$ [µm] | $B_O$ [µm] | $L_B$ [µm] | $B_B$ [µm] | $T$ [µm] | $\alpha$ [1] |
|---|---|---|---|---|---|---|
| BO1 | 1200 | 2400 | 2400 | 600 | 24.5 | 0.36 |
| BO2 | 1800 | 2400 | 1800 | 600 | 24 | 0.27 |
| BO3 | 2400 | 1800 | 1200 | 600 | 17 | 0.47 |
| PO1 | 1200 | 2400 | 2400 | 600 | 24 | 0.45 |
| PO1_100 [1] | 1200 | 2400 | 2400 | 600 | 21 | 0.30 |
| PO2 | 1800 | 2400 | 1800 | 600 | 27 | 0.34 |
| PO2_100 [1] | 1800 | 2400 | 1800 | 600 | 27 | 0.30 |
| CO1_33 [1] | 3600 | 2400 | - | - | 12 | 0.84 |
| CO1_50 [1] | 3600 | 2400 | - | - | 12 | 0.58 |
| CO1_100 [1] | 3600 | 2400 | - | - | 8.5 | 0.61 |
| CO2_33 [1] | 3600 | 1800 | - | - | 12 | 0.95 |
| CO2_100 [1] | 3600 | 1800 | - | - | 9 | 0.67 |

[1] The value is indicating the percentage of coverage of the oscillator surface [30].

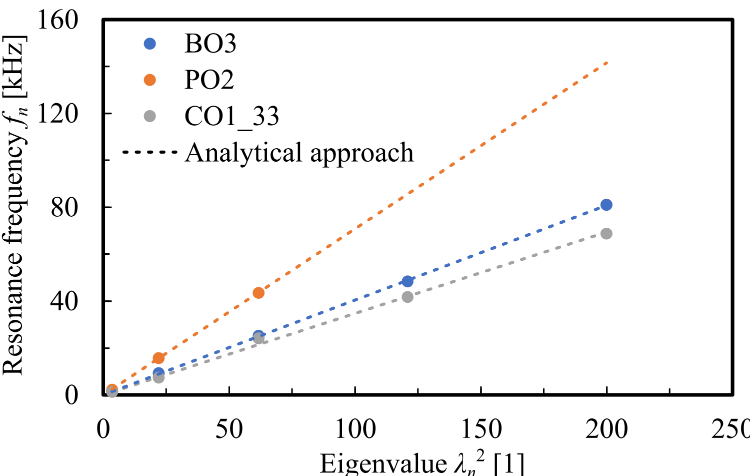


**Figure 5.** Exemplary resonance frequency plot of three oscillator geometries dependent on the eigenvalue. Additionally, the analytical calculation according to Equation (3) is included, which shows a very good agreement. Mode 4 and 5 of micro-oscillator PO2 were electrically not measurable with the piezoelectric elements because the deflection is not in the area of the sensing patches.

In the following, the resonance frequencies of the fundamental mode and the higher bending modes are plotted against the squared eigenvalue $\lambda_n$. By means of the scaling factor $\alpha$, Equation (3) is fitted to the measurement points using the best fit method. Figure 5 shows this exemplarily for a MEMS oscillator of each geometric shape and indicates a very good agreement with the analytical approach. The determined scaling values are listed in Table 1. It is noticeable that the CO structures have the largest values. This is since the oscillator and the bending beam are congruent to each other. The dependence can also be observed on the coverage size. A larger actuator area counteracts the oscillation because the stress of the piezoelectric layer has an additional restoring effect. The smallest possible actuator area thus represents the ideal case of a fully oscillating structure.

For the BO and PO structures, on the other hand, the oscillating mass is mainly given by the oscillator plate dimension itself which is actuated via the beam structure. The larger the beam structure, the smaller the fraction of oscillating mass, after which the scale factor $\alpha$ decreases. Regarding the size of the coverage of the oscillator with the actuator surface, the same observation can be seen for the CO structures. The completely covered structures PO1_100 and PO2_100 show a lower scaling factor $\alpha$ than the regular structures PO1 and PO2.

In the following section, the determined parameters obtained by the fitting procedure shown in Figure 3 will be discussed. In Figure 6, the fitting parameters are depicted as a function of the gap width. The parameters of the individual damping mechanisms show an increase with the gap width which leads to saturation for larger values of the gap width. The molecular fit parameter $\xi_{\text{mol}}$ has already been discussed in a previous paper [25] and is excluded in the following. The parameters of the transitional flow regime ($\xi_{\text{trans}}$, $B_{trans}$) and the viscous flow regime ($\xi_{\text{vis}}$) are fitted with the following function which describes an upward limited growth function:

$$\xi(h) = \xi_{\text{sat}} \cdot \left(1 - e^{-\frac{h}{l^*}}\right). \tag{10}$$

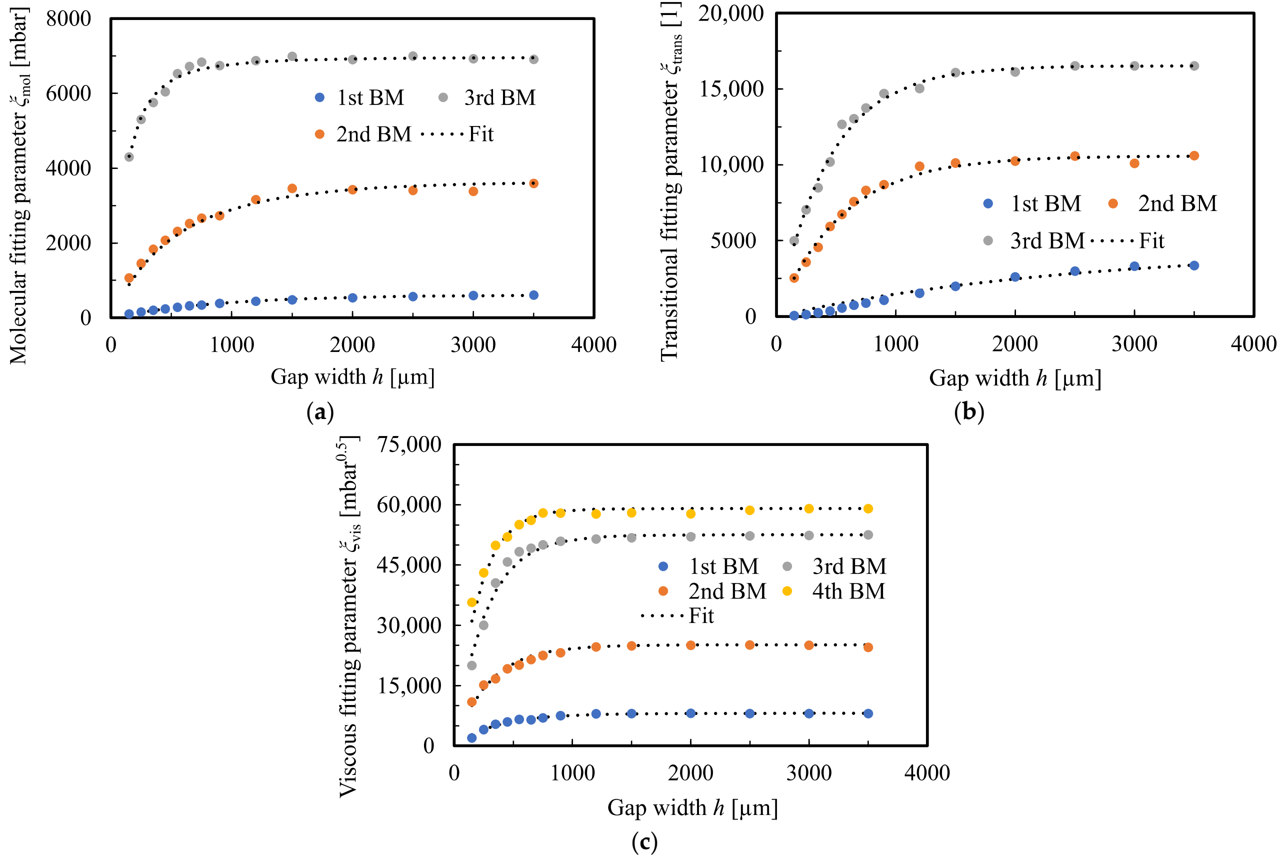


**Figure 6.** The determined fit parameters for MEMS oscillator BO3 of the higher bending modes as a function of the gap width. In (**a**) the curve is shown for the molecular fitting parameter, in (**b**) for the transitional fitting parameter, and in (**c**) for the viscous fitting parameter. Each plot was fitted by an upward limited exponential growth function to determine the characteristic length (*cf.* Equation (10)).

The course is determined by the saturation value $\xi_{sat}$, which represents the horizontal asymptote of the function and by the characteristic length $l^*$, which describes the speed of the increase of the gap width.

## 5. Discussion

By applying the generalized fit model, the quality factor plots of three different geometric shapes with different dimensions were fitted from the molecular to the viscous flow range and simultaneously for gap widths to a geometric boundary varying from 150 μm up to 3500 μm. As shown in the previous section, fit parameters were obtained that exhibit a gap width dependence, which can be described according to Equation (10). The determined quantities, the saturation value, and the characteristic length are analyzed in more detail in the following.

In Figure 7, the characteristic lengths for the viscous and thermal damping are depicted. These characteristic lengths represent the range of the interaction with the geometrical boundary. A gap width in the range of the characteristic length thereby means an increase in the quality factor by 63% (=$1 - e^{-1}$) of the saturation value of a freely oscillating structure.

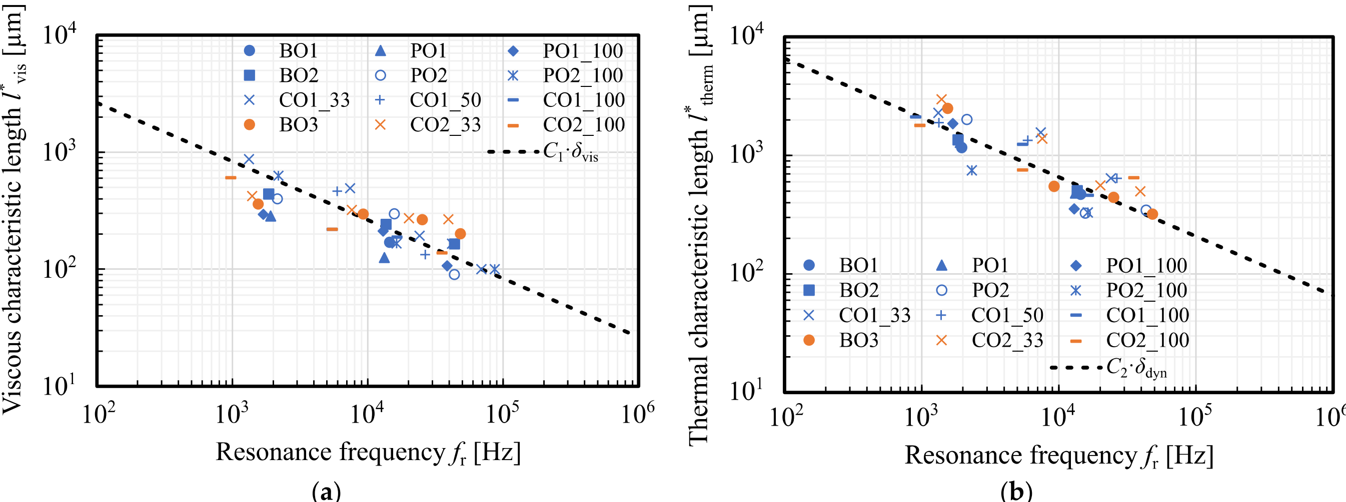


**Figure 7.** Determined characteristic length of the viscous damping (**a**) as well as of the thermodynamic damping of the transitional flow regime (**b**). In both cases, a multiple of the viscous or thermal boundary layer thickness is included ($C_1$ = 12, $C_2$ = 25).

At a distance larger than three times the characteristic length, the damping has dropped to 5% of the original value. Thus, knowledge of the ratio of the distance characteristic can be taken as a measure of the strength of the damping.

In Figure 7, a multiple of the viscous $\delta_{vis}$ and the thermal $\delta_{dyn}$ boundary layer thickness is inserted, which are given as a function of the frequency $f$ by the following equations [31]:

$$\delta_{\text{vis}}(f) = \sqrt{\frac{\mu}{\pi \rho f}} \tag{11}$$

$$\delta_{\text{dyn}}(f) = \sqrt{\frac{k}{\pi \rho C_p f}}, \tag{12}$$

with $\mu$, $\rho$, $k$, $C_p$ the dynamic viscosity, the density, the thermal conductivity, and the heat capacity at constant pressure, respectively. The gas properties for the fitting of the boundary layer thicknesses were taken from NIST [32].

For the viscous damping, we find a characteristic length $l^*_{vis}$ in the order of $C_1$ = 8–15 times the viscous boundary layer thickness depending on the MEMS oscillator and a mean value of 12. A similar consideration of the damping of the thermal resonance effects in the transitional flow regime yields to a thermal characteristic length $l^*_{therm}$ in the range of $C_2$ = 20–30 times the thermal boundary layer thickness also depending on the exact oscillator geometry with a mean value of about 25. Thus, the thermal effects are generally more long-range than the viscous losses. Furthermore, the decrease in the characteristic length with frequency is observed which agrees with the FEM simulations (*cf.* Figure 2). A higher mode or frequency interacts more short-range with a geometric boundary than the fundamental mode at a lower frequency.

At large distances, a saturation value is obtained, which represents the ideal case of free oscillatory movement without the influence of spatial constraints. In Figure 8, the saturation value for the thermal damping is illustrated. The measurement values clearly distinguish a difference between the MEMS oscillators regarding their width (Blue $B_O$ = 2400 µm; Orange $B_O$ = 1800 µm). The overall trend can be described by a logarithmic function which correlates with a strong decrease in the thermal damping with the frequency. Thermal resonance effects are therefore particularly pronounced at low frequencies or in the fundamental mode.

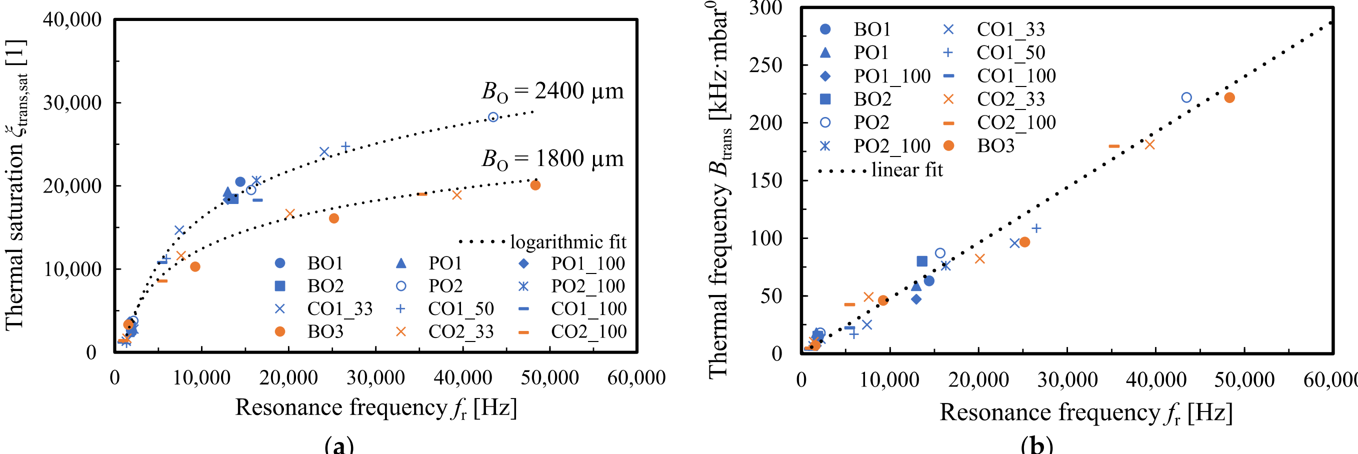


**Figure 8.** Saturation values of the thermodynamic damping for large gap widths determined according to Equation (10) (**a**). The data of the MEMS oscillators show a good agreement with a logarithmic function. The graph reveals two groups that differ in the width of the oscillators $B_O$. The thermodynamic resonance frequency is determined by the fit parameter $B_{dyn}$ which shows an almost linear trend to the resonance frequency of the oscillator (**b**).

The pressure-dependent factor of the thermal resonance frequency shows a linear dependence on the mechanical resonance frequency (see Figure 8b). This derives from the fact that the thermal and mechanical resonance frequencies match at a specific pressure, which we define as the thermal resonance pressure.

The viscous saturation value is predicted by various theories of a freely vibrating structure in a viscous medium. The resulting dependence of the viscous quality on the reciprocal root of the resonant frequency is plotted in Figure 9 and reflects the general trend of the measurements. The individual MEMS oscillators differed in strength from each other due to the different geometries. It is noticeable that the cantilever structures have the highest damping. The further sorting is carried out according to the size of the surface of the MEMS oscillators after which only the absolute area of interaction with the viscous medium is decisive. This is different from damping in liquids where the perimeter of the edges and thus additional slits and edges are counterproductive. According to Basak et al., additional edges lead to turbulence effects which decrease the quality factor [33].

The last point to be investigated is the intrinsic quality factor. All data are summarized in Appendix C and plotted in Figure 9b as a function of the resonance frequency. Several points are noticeable as a result. First, a larger beam structure leads to higher losses via the anchor. For this reason, the cantilever structures have the lowest intrinsic values. The BO and PO structures are sorted by their beam width. On the other hand, larger piezoelectric actuator films also have a negative effect on intrinsic quality. Up to a frequency of about 30 kHz, the quality factor increases approximately linearly with resonance frequency for all structures. At higher frequencies, the thermoelastic damping mechanism is dominant, which leads to a decrease in the intrinsic Q-factor [34]. In general, it can be concluded that the intrinsic quality factor can be improved with the smallest possible actuator area and minimal anchor structures.

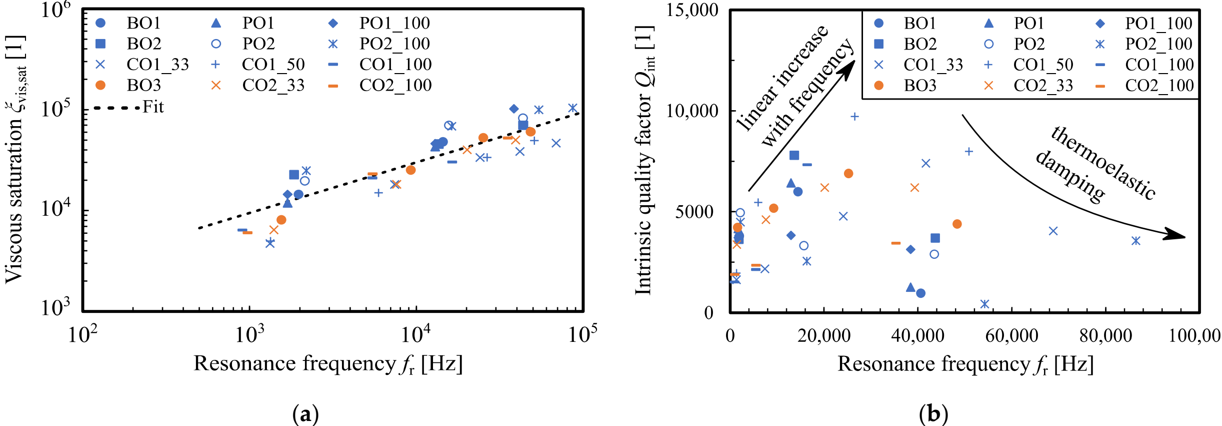


**Figure 9.** Viscous saturation values for large gaps of all investigated MEMS oscillators as a function of resonance frequency (**a**). The plotted fit line shows the dependence of the quality factor on the frequency in the viscous flow regime according to Equation (8). In (**b**), the intrinsic quality factors of all MEMS oscillators as well as all determined bending modes measured in the high vacuum range at a pressure level of 0.001 mbar are shown.

## 6. Conclusions

A generalized damping model based on the literature results for individual damping mechanisms was presented. First, an analytical description of the resonance frequency was presented, which is in good agreement with the experimental results for all considered geometries and allows numerical determination of the thickness *T*. The quality factor could be reproduced by superposition of four components for the three different oscillator geometries (BO, PO, CO) over six orders of magnitude of the Knudsen number *Kn*. The results of the fitting procedure were further analyzed and interpreted using FEM simulations. From these results, the pressure and temperature distributions within the gap caused by the micro-oscillator movement were obtained. The thermal and viscous interaction with the boundary was visualized and a decrease in the range of the effects with the resonance frequency and the mode number was observed. The decrease in the influence of the damping phenomena was also found experimentally and described with a saturation behavior, from which a characteristic length was obtained, which was used for the estimation of the range of the effects. From these results, indications for reducing the damping were found, thus giving opportunities for increasing the quality factor. Furthermore, the influence of a geometrical boundary due to the package or the mounting can be predicted. The results are briefly summarized below:

- The range of viscous damping is about 8–15 times the viscous boundary layer thickness.
- The measure of the strength is the surface which interacts with the viscous fluid and decreases with the resonance frequency.
- The range of thermal effects in the transitional flow regime is about 20–30 times the thermal boundary layer thickness.
- Exponential decreasing of thermal damping effects occurs with an increase in resonance frequency.
- The thermal resonance frequency of the gas depends linearly on the mechanical resonance frequency of the micro-oscillator.
- The intrinsic quality factor of the fundamental mode is limited by anchor losses and residual stress of the piezoelectric thin film. Therefore, the minimization of an anchor structure and the actuator area are recommended to maximize the intrinsic quality factor.
- At higher modes, thermoelastic damping is crucial, which leads to a lowering of the intrinsic quality of higher modes.

With this model, we give an approach to describing the resonance frequency and quality factor of various MEMS oscillators as well as optimization possibilities to improve the performance of piezoelectric-actuated oscillators.

**Author Contributions:** Investigation, T.Z.; Data curation, T.Z.; Project administration A.A. and H.S.; Funding acquisition A.A. and H.S., Writing—original draft T.Z. and H.S.; Writing—review and editing, T.Z. and H.S. All authors have read and agreed to the published version of the manuscript.

**Funding:** This research was funded by the German Science Foundation (DFG) within the grant SE 1425/14-1.

**Institutional Review Board Statement:** Not applicable.

**Informed Consent Statement:** Not applicable.

**Data Availability Statement:** Data available on request.

**Conflicts of Interest:** The authors declare that there are no conflict of interest.

## Appendix A

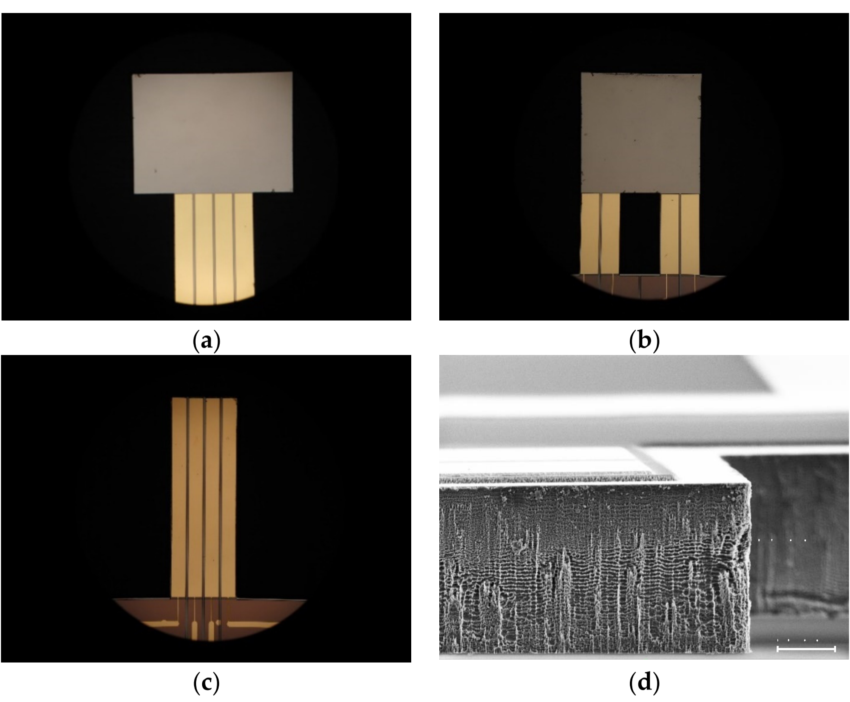

**Figure A1.** Microscopic image of the three different micro-oscillator structures: PO (**a**), BO (**b**), and CO (**c**) and a scanning electron microscope image illustrating the side view on a micro-oscillator revealing a thickness of 27 µm (**d**).

## Appendix B

The micro-oscillators were fabricated as shown in the cross-sectional view depicted in Figure A2a. A highly p-doped 4″ Si-wafer with a thickness of 525 µm was used as substrate. In the first step, $SiO_2$ was grown with a thickness of 120 nm on both sides for electrical insulation and as a bonding agent of the $Si_3N_4$ layer. The $Si_3N_4$ layer was deposited in a PECVD process in a thickness of 550 nm and was used as a passivation layer for the anisotropic KOH etching step to release the micro-oscillators. Both layers were structured simultaneously in a 6% HF solution. Next, the piezoelectric thin film was deposited in a reactive sputter deposition process in a thickness of 1100 nm and etched with phosphoric acid solution after a photolithographic structuring step. Subsequently, the piezoelectric elements are connected with a 500 nm thick Au layer using a DC sputtering process. The Au film is structured by an etching step with aqua regia. Afterward, the micro-oscillators

are released in a two-step process. Firstly, a thin membrane is etched anisotropically from the backside in a KOH etching solution, and released by a DRIE step (Bosch-process) from the top side. Before the DRIE process, the KOH cavities are filled with photoresists to mechanically stabilize the oscillator and to stop the DRIE etching process. The photoresist is removed after the dicing of the wafer within the cleaning process of the individual chips. Finally, the micro-oscillators are glued on PCB-boards to contact them electrically via Au bond wires. The PCB boards are drilled in advance at the locations of the micro-oscillator so that they are not confined to the bottom.

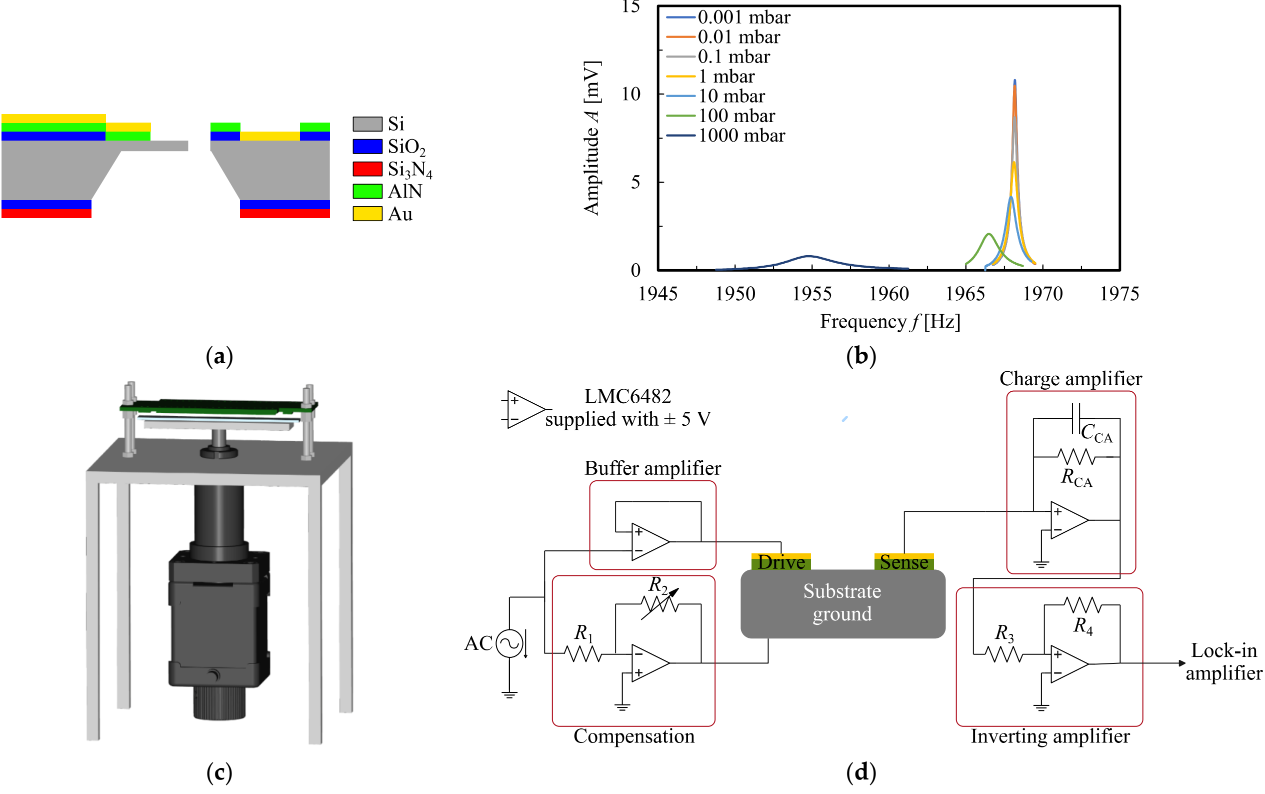


**Figure A2.** Cross-sectional view on a micro-oscillator (layer thickness are not to scale) (**a**), and recorded resonance curves of BO1 (**b**) for various ambient pressure levels. In (**c**), the construction for adjusting the gap width to the neighboring plate is depicted, and in (**d**) the electric circuit for the actuation and detection of the micro-oscillators.

The quality factor and resonance frequency of the micro-oscillators as shown in Figures 3–5 are measured by recording the resonance curves sown in Figure A2b for various ambient pressure conditions. Therefore, the micro-oscillators are placed in a vacuum chamber ranging from $10^{-3}$ mbar up to 900 mbar. Additionally, the PCB board containing four micro-oscillators is built in a construction shown schematically in Figure A2c to adjust the gap width to the neighboring plate. The distance between the plate and the micro-oscillator is initially calibrated with two cooper gauge blocks with a defined thickness of 800 µm. The actuation of the micro-oscillator and the sensing of the oscillation are achieved with the electric circuit illustrated in Figure A2d. The micro-oscillators are actuated with a sinusoidal signal with an amplitude of 1 V which is decoupled by a buffer amplifier. The electrical crosstalk between actuation and sensing is compensated by a shift of the substrate ground [35]. The amplitude of the oscillation movement is measured by collecting the charge of the sensing elements with a charge amplifier which amplifies the signal and converts it in the range of a few µV. Finally, this signal is lifted to several mV by an inverting amplifier. Then, the actuation and sensing signal is compared by a lock-in amplifier and evaluated regarding their amplitude and phase.

## Appendix C

| Name | $L_O$ [µm] | $B_O$ [µm] | $L_B$ [µm] | $B_B$ [µm] | $T$ [µm] | $\alpha$ [1] | Mode | $f_n$ [kHz] | $Q_{int}$ [1] |
|---|---|---|---|---|---|---|---|---|---|
| BO1 | 1200 | 2400 | 2400 | 600 | 24.5 | 0.36 | 1st BM | 1.97 | 3805 |
| | | | | | | | 2nd BM | 14.3 | 6002 |
| | | | | | | | 3rd BM | 40.6 | 965 |
| BO2 | 1800 | 2400 | 1800 | 600 | 24 | 0.27 | 1st BM | 1.85 | 3640 |
| | | | | | | | 2nd BM | 13.6 | 7800 |
| | | | | | | | 3rd BM | 43.7 | 3704 |
| BO3 | 2400 | 1800 | 1200 | 600 | 17 | 0.47 | 1st BM | 1.55 | 4230 |
| | | | | | | | 2nd BM | 9.24 | 5175 |
| | | | | | | | 3rd BM | 25.2 | 6905 |
| | | | | | | | 4th BM | 48.3 | 4402 |
| PO1 | 1200 | 2400 | 2400 | 600 | 24 | 0.45 | 1st BM | 1.92 | 4170 |
| | | | | | | | 2nd BM | 13.2 | 6436 |
| | | | | | | | 4th BM | 69.7 | 1272 |
| PO1_100 | 1200 | 2400 | 2400 | 600 | 21 | 0.30 | 1st BM | 1.69 | 3722 |
| | | | | | | | 2nd BM | 13.0 | 3832 |
| | | | | | | | 3rd BM | 38.4 | 3133 |
| PO2 | 1800 | 2400 | 1800 | 600 | 27 | 0.34 | 1st BM | 2.15 | 4951 |
| | | | | | | | 2nd BM | 15.7 | 3326 |
| | | | | | | | 3rd BM | 43.4 | 2898 |
| PO2_100 | 1800 | 2400 | 1800 | 600 | 27 | 0.30 | 1st BM | 2.11 | 4488 |
| | | | | | | | 2nd BM | 16.3 | 2555 |
| | | | | | | | 3rd BM | 54.2 | 431 |
| | | | | | | | 4th BM | 86.4 | 3571 |
| CO1_33 | 3600 | 2400 | - | - | 12 | 0.84 | 1st BM | 1.33 | 1635 |
| | | | | | | | 2nd BM | 7.40 | 2174 |
| | | | | | | | 3rd BM | 24.1 | 4781 |
| | | | | | | | 4th BM | 41.7 | 7404 |
| | | | | | | | 5th BM | 68.8 | 4050 |
| CO1_50 | 3600 | 2400 | - | - | 12 | 0.58 | 1st BM | 1.34 | 1956 |
| | | | | | | | 2nd BM | 5.94 | 5459 |
| | | | | | | | 3rd BM | 26.5 | 9718 |
| | | | | | | | 4th BM | 50.9 | 7995 |
| CO1_100 | 3600 | 2400 | - | - | 8.5 | 0.61 | 1st BM | 0.90 | 1519 |
| | | | | | | | 2nd BM | 5.45 | 2140 |
| | | | | | | | 3rd BM | 16.4 | 7337 |
| | | | | | | | 4th BM | 34.8 | 4002 |
| CO2_33 | 3600 | 1800 | - | - | 12 | 0.95 | 1st BM | 1.40 | 3371 |
| | | | | | | | 2nd BM | 7.59 | 4614 |
| | | | | | | | 3rd BM | 20.2 | 6199 |
| | | | | | | | 4th BM | 39.3 | 6198 |
| CO2_100 | 3600 | 1800 | - | - | 9 | 0.67 | 1st BM | 0.97 | 1896 |
| | | | | | | | 2nd BM | 5.47 | 2350 |
| | | | | | | | 4th BM | 35.3 | 3448 |

## References


1. Pillai, G.; Li, S. Piezoelectric MEMS resonators: A review. *IEEE Sens. J.* **2021**, *21*, 12589–12605. [CrossRef]
2. Weng, C.; Pillai, G.; Li, S. A thin-film piezoelectric-on-Silicon MEMS oscillator for mass sensing applications. *IEEE Sens. J.* **2020**, *12*, 7001–7009. [CrossRef]
3. Zengerle, T.; Stopp, M.; Ababneh, A.; Seidel, H. Using the nonlinear Duffing effect of piezoelectric micro-oscillators for wide-range pressure sensing. *Actuators* **2021**, *10*, 172. [CrossRef]
4. Ruiz-Diez, V.; Toledo, J.; Hernando-Garcia, J.; Ababneh, A.; Seidel, H.; Sanchez-Rojas, J. A geometrical study on the roof tile-shaped modes in AlN-based piezoelectric microcantilevers as viscosity–density sensors. *Sensors* **2019**, *19*, 658. [CrossRef]
5. van Beek, J.; Puers, R. A review of MEMS oscillators for frequency reference and timing applications. *J. Micromech. Microeng.* **2012**, *22*, 1–35. [CrossRef]
6. Kim, B.; Melamud, R.; Candler, R.; Hopcroft, A.; Jha, C.; Chandorkar, S.; Kenny, T. Encapsulated MEMS resonators—A technology path for MEMS into frequency control applications. In Proceedings of the IEEE International Frequency Control Symposium, Newport Beach, CA, USA, 1–4 June 2010; pp. 1–4.
7. Tu, C.; Lee, J.; Zhang, X. Dissipation analysis methods and Q-enhancement strategies in piezoelectric MEMS laterally vibrating resonators: A review. *Sensors* **2020**, *20*, 4978. [CrossRef] [PubMed]
8. Xu, C.; Piazza, G. Active boost in the quality factor of an AlN MEMS resonator up to 165,000. In Proceedings of the IEEE 32nd International Conference on Micro Electro Mechanical Systems (MEMS), Seoul, South Korea, 27–31 January 2019; pp. 907–910.
9. Haider, S.; Saleem, M.; Ahmed, M. Effect of environmental conditions and geometric parameters on the squeeze film damping in RF-MEMS switches. *AICPEF* **2019**, *100*, 357–368. [CrossRef]
10. Patocka, F.; Schneidhofer, C.; Dörr, N.; Schneider, M.; Schmid, U. Novel resonant MEMS sensor for the detection of particles with dielectric properties in aged lubricating oils. *Sens. Actuators A* **2020**, *315*, 112290. [CrossRef]
11. Kim, B.; Melamud, R.; Candler, R.; Hopcroft, M.; Kenny, T. MEMS packaging for reliable resonators and oscillators. In Proceedings of the IEEE/MTT-S International Microwave Symposium, Montreal, QC, Canada, 17–22 June 2012; pp. 1–3.
12. Brown, J.; Lutz, M.; Partridge, A.; Gupta, P.; Radza, E. MEMS as low-cost high-volume semiconductor solutions: It's all in the packaging and assembly. *SPIE MOEMS-MEMS* **2008**, *6884*, 183–188.
13. Karniakadis, G.; Beskok, A.; Aluru, A. *Microflows and Nanoflows: Fundamentals and Simulation*, 1st ed.; Springer: New York, NY, USA, 2005.
14. Zengerle, T.; Joppich, J.; Schwarz, P.; Ababneh, A.; Seidel, H. Modeling the damping mechanism of MEMS oscillators in the transitional flow regime with thermal waves. *Sens. Actuators A* **2020**, *311*, 112068. [CrossRef]
15. Alrasheed, S. Oscillatory motion. In *Principles of Mechanics*, 1st ed.; Springer International Publishing: Cham, Switzerland, 2019; pp. 155–171.
16. Young, W.; Budynas, R. *Roark's Formulas for Stress and Strain*, 7th ed.; McGraw-Hill Professional: New York, NY, USA, 2001; pp. 799–812.
17. Boisen, A.; Dohn, S.; Keller, S.; Schmid, S.; Tenje, M. Cantilever-like micromechanical sensors. *Rep. Prog. Phys.* **2011**, *74*, 3. [CrossRef]
18. Timoshenko, S.; Young, D.; Weaver, W. *Vibration Problems in Engineering*, 4th ed.; Wiley: New York, NY, USA, 1974.
19. Petersan, P.; Anlage, S. Measurement of resonant frequency and quality factor of microwave resonators: Comparison of methods. *J. Appl. Phys.* **1998**, *84*, 3392–4002. [CrossRef]
20. Rodriguez, J.; Chandorkhar, S.; Glaze, G.; Gerrard, D.; Chen, Y.; Heinz, D.; Flader, I.; Kenny, T. Direct detection of anchor damping in MEMS tuning fork resonators. *J. Microelectromech. Syst.* **2018**, *27*, 800–809. [CrossRef]
21. Qiu, H.; Ababneh, A.; Feili, D.; Wu, X.; Seidel, H. Analysis of intrinsic damping in vibrating piezoelectric microcantilevers. *Microsyst. Technol.* **2016**, *22*, 2017–2025. [CrossRef]
22. Zener, C. Internal friction in solids: II. General theory of thermoelastic internal friction. *Phys. Rev.* **1937**, *53*, 90–99. [CrossRef]
23. Christian, R. The theory of oscillating-vane vacuum gauges. *Vacuum* **1966**, *16*, 175–178. [CrossRef]
24. Bao, M.; Yang, H.; Yin, H.; Sun, Y. Energy transfer model for squeeze-film air damping in low vacuum. *J. Micromech. Microeng.* **2002**, *12*, 341–346. [CrossRef]
25. Zengerle, T.; Joppich, J.; Schwarz, P.; Ababneh, A.; Seidel, H. Polyatomic degrees of freedom and their temporal evolution extracted from the damping of micro-oscillators. *Sens. Actuators A* **2019**, *297*, 111460. [CrossRef]
26. Kokubun, K.; Hirata, M.; Ono, M.; Murakami, H.; Toda, Y. Unified formula describing the impedance dependence of a quartz oscillator on gas pressure. *J. Vac. Sci. Technol. A* **1987**, *5*, 2450–2453. [CrossRef]
27. Blom, F.; Bouwstra, S.; Elwenspoek, M.; Fluitman, J. Dependence of the quality factor of micromachined silicon beam. *J. Vac. Sci. Technol. B* **1992**, *10*, 341–346. [CrossRef]
28. Kurmendra, S.; Kumar, R. Design analysis, modeling and simulation of novel rectangular cantilever beam for MEMS sensors and energy harvesting applications. *Int. J. Inf. Technol.* **2017**, *9*, 295–302. [CrossRef]
29. Hopcroft, M.; Nix, W.; Kenny, T. What is the Young's modulus of silicon? *J. Microelectromech. Syst.* **2010**, *3*, 229–238. [CrossRef]
30. Zengerle, T.; Stopp, M.; Ababneh, A.; Seidel, H. Investigations on nonlinearities of roof tile-shape modes for pressure measurement applications. In Proceedings of the 21st International Conference on Solid-State Sensors, Actuators and Microsystems (Transducers), Orlando, FL, USA, 20–24 June 2021; pp. 1343–1346.

31. Qiu, H.; Seidel, H. Hydrodynamic loading on vibrating piezoelectric microresonators. In *Piezoelectricity–Organic and Inorganic Materials and Applications*, 1st ed.; IntechOpen Limited: London, UK, 2018; pp. 43–64.
32. Lemmon, E.; McLinden, M.; Friend, D. Thermophysical Properties of Fluid Systems NIST. 1998. Available online: https://webbook.nist.gov/chemistry/fluid/ (accessed on 10 February 2022).
33. Basak, S.; Raman, A.; Garimella, S. Hydrodynamic loading of microcantilevers vibrating in viscous fluids. *J. Appl. Phys.* **2006**, *99*, 114906. [CrossRef]
34. Duwel, A.; Candler, R.; Kenny, T.; Varghese, M. Engineering MEMS resonators with low thermoelastic damping. *J. Microelectromech. Syst.* **2006**, *15*, 1437–1445. [CrossRef]
35. Qiu, H.; Schwarz, P.; Völlm, H.; Feili, D.; Wu, X.; Seidel, H. Electrical crosstalk in two-port piezoelectric resonators and compensation solutions. *J. Micromech. Microeng.* **2013**, *23*, 4. [CrossRef]